Broadband extended image gathers from joint inversion of multiple, simultaneous-source wavefields

Ivan Vasconcelos* and James Rickett, Schlumberger Gould Research.

Abstract

We propose a method for inversion of subsurface reflectivity image gathers that jointly relies on the broadband nature of combining multiple wavefields with diverse temporal and spatial spectra. Our inversion retrieves depth-domain extended images (EIs), which represent the full reflectivity operators within the subsurface. Based on interferometry by multidimensional deconvolution (MDD), we present MDD-based imaging conditions for an extended-image inversion. Our method consists of deconvolving correlation-based EIs with the so-called joint point-spread function (JPSF). This method can account for imaging primaries as well as internal and free-surface multiples. Because it is based on MDD, our JPSF approach can account for blended/simultaneous-source data in imaging with no need to separate the simultaneous-source data prior to imaging. With the example dual-source vector-acoustic seismic data the extended-image JPSF system is constructed by separating source and receiver wavefields from upgoing and ghost data, from both pressure and gradient sources. We demonstrate how the method inverts for EIs representing subsurface reflectivity, while benefiting from the increase in temporal and spatial bandwidth brought on by dual-source multimeasurement data. In addition, our joint wavefield approach provides a framework for jointly imaging data from multiple experiments of any kind (e.g., surface and borehole, active and passive).

Introduction

Imaging and inversion in highly complex subsurface often calls for the generation of depth-domain image gathers. The so-called extended images (EIs, Vasconcelos et al., 2010) represent time-varying reflectivity responses between pseudosources and pseudoreceivers placed within the subsurface and can be used for velocity analysis but can also represent localized reflectivity responses useful for reservoir characterization. Here we build on the multidimensional deconvolution (MDD) approach to seismic interferometry presented by van der Neut et al. (2010) and Wapenaar et al. (2012) to design an MDD-based method of inverting for EIs that jointly combines multiple wavefield experiments. With the example of blended dual-source, vector-acoustic seismic data, we discuss how this new method retrieves EIs that are both spatially and temporally broadband.

Extended-image inversion with joint point-spread functions

An EI can be defined as $I_e(\mathbf{x}_d, \mathbf{x}_z, \tau) = R_0^+(\mathbf{x}_d, \mathbf{x}_z, \tau)$, i.e., the subsurface reflectivity response for a pseudosource at $\mathbf{x}_z$ and pseudoreceiver at $\mathbf{x}_d$ at a given time τ (Vasconcelos et al., 2010). In the subsurface, the frequency-domain up- and downgoing fields, $\hat{p}^-$ and $\hat{p}^+$, are related through $\hat{R}_0^+$ by using $\hat{\mathbf{P}}^- = \hat{\mathbf{R}}_\mathbf{0}^+ \hat{\mathbf{P}}^+$, where $\hat{\mathbf{P}}^-$ has elements $\hat{p}^-(\mathbf{x}_d, \mathbf{x}_s)$ and $\hat{\mathbf{P}}^+$ has elements $\hat{p}^+(\mathbf{x}_z, \mathbf{x}_s)$, with the $\mathbf{x}_s$ source locations in the column space. Alternatively, the wavefield-matrix system can be recast in terms of the normal equations

$$\hat{\mathbf{C}} = \hat{\mathbf{R}}_\mathbf{0}^+ \hat{\Gamma} \tag{1}$$

with $\hat{\mathbf{C}} = \hat{\mathbf{P}}^- \left(\hat{\mathbf{P}}^+\right)^\dagger$ and $\hat{\Gamma} = \hat{\mathbf{P}}^+ \left(\hat{\mathbf{P}}^+\right)^\dagger$, where † denotes the conjugate transpose matrix. After van der Neut et al. (2010), $\hat{\Gamma}$ is hereafter referred to as a wavefield point-spread function (PSF). In the case of image-domain inversion, the matrix $\hat{\mathbf{C}}$ is the collection of all correlation-based extended image gathers at a target datum (Vasconcelos et al., 2010). In the imaging case, equation 1 states that the correlation-based EI gathers $\hat{\mathbf{C}}$ *are* the reflectivity operator blurred by $\hat{\Gamma}$, the wavefield PSF.

Unlike the interferometry applications as in van der Neut et al. (2010) and Wapenaar et al. (2011), where the fields in the matrices $\hat{\mathbf{P}}^{+,-}$ come from direct observations, for our imaging applications $\hat{\mathbf{P}}^+$ is the so-called source wavefield (Vasconcelos et al., 2010; Sava and Vasconcelos, 2011), obtained by forward modeling using a known model, and $\hat{\mathbf{P}}^-$ is the subsurface receiver wavefield obtained by extrapolation of the recorded surface data. For the purposes of this paper, we assume that the extrapolation process is "ideal" in the sense that it yields subsurface receiver wavefields $\hat{\mathbf{P}}^{+,-}$ that closely correspond to observed fields, should those be available.

For broadband applications, here we extend the PSF system for extended images in equation 1 to account for multiple wavefields: these may correspond to different experiments altogether (e.g., surface seismic, OBC, VSP), different source excitations and/or locations, passive and active data, etc. In this context, let $\hat{\mathbf{P}}_{(1)}^{-,+}$ to $\hat{\mathbf{P}}_{(N)}^{-,+}$ be N separate sets of up- and downgoing wavefields from N different experiments, but that correspond to the same subsurface. In that case, we can combine these wavefields

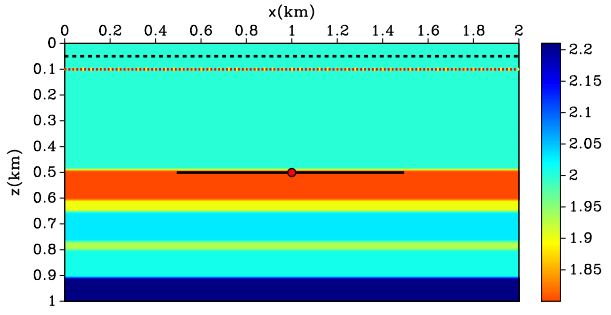

Figure 1: Model used in the numerical example. Source locations lie on the dashed black line, with 20-m spacing. Each shot is recorded by receivers placed on the red dashed line, with 10-m spacing. The red dot at 0.5-km depth shows the location of a reference image point $\mathbf{x}$, and the black line denotes the extension of horizontal lags $\delta\mathbf{x}$ in the image gathers. The colorbar shows wavespeed in km/s.

into joint wavefield block matrices $\hat{\mathbf{P}}_J^{-,+}$, yielding

$$\underbrace{\begin{bmatrix} w_1\hat{\mathbf{P}}^-_{(1)} \\ w_2\hat{\mathbf{P}}^-_{(2)} \\ \cdots \\ w_N\hat{\mathbf{P}}^-_{(N)} \end{bmatrix}^T}_{\hat{\mathbf{P}}_J^-} = \hat{\mathbf{R}}^+_{\mathbf{0,J}} \underbrace{\begin{bmatrix} w_1\hat{\mathbf{P}}^+_{(1)} \\ w_2\hat{\mathbf{P}}^+_{(2)} \\ \vdots \\ w_N\hat{\mathbf{P}}^+_{(N)} \end{bmatrix}^T}_{\hat{\mathbf{P}}_J^+}, \tag{2}$$

where $w_1(\omega)$ through $w_N(\omega)$ are frequency-dependent scalar weights, which are chosen according to any desired criteria (see Example section). We have then have the system $\hat{\mathbf{C}}_J = \hat{\mathbf{R}}^+_{\mathbf{0}}\hat{\Gamma}_J$, where $\hat{\mathbf{C}}_J = \hat{\mathbf{P}}_J^-\left(\hat{\mathbf{P}}_J^+\right)^\dagger$ and $\hat{\Gamma}_J = \hat{\mathbf{P}}_J^+\left(\hat{\mathbf{P}}_J^+\right)^\dagger$. Note that in this system, $\hat{\Gamma}_J$ is the PSF of the joint wavefield system, which we refer to as the joint PSF matrix, or JPSF. It also follows from equation 2 that

$$\underbrace{\sum_{i=1}^{N} w_i^2\hat{\mathbf{C}}_{(i)}}_{\hat{\mathbf{C}}_J} = \hat{\mathbf{R}}^+_{\mathbf{0}}\underbrace{\left(\sum_{i=1}^{N} w_i^2\hat{\Gamma}_{(i)}\right)}_{\hat{\Gamma}_J}. \tag{3}$$

which shows that combining wavefields in the column space as in equation 2 results in a JPSF system with the same dimensions as that for a single experiment (equation 1): the joint matrices $\hat{\mathbf{C}}_J$ and $\hat{\Gamma}_J$ are simply the weighted superposition of the $\hat{\mathbf{C}}_{(i)}$ and $\hat{\Gamma}_{(i)}$ from each experiment. The inverted EIs are obtained from the JPSF system by means of MDD:

$$\widehat{\mathbf{R}}^+_{\mathbf{0,LS}} = \hat{\mathbf{C}}_J\hat{\Gamma}_J^\ddagger, \tag{4}$$

where $\widehat{\mathbf{R}}^+_{\mathbf{0,LS}}$ denotes a least-squares estimate of $\widehat{\mathbf{R}}^+_{\mathbf{0}}$, and $\hat{\Gamma}_J^\ddagger$ represents a pseudoinverse of $\hat{\Gamma}_J$, obtained by, e.g., Tikhonov regularization, truncated SVD, and others. The imaging condition in equation 4 states that the reflectivity EI is obtained by the multichannel deconvolution of the correlation-based EI for the joint wavefields with the JPSF $\hat{\Gamma}_J$.

Extended images from blended wavefields

For the case of blended, or simultaneous-source data, we follow the same notation as Wapenaar et al. (2012) in defining up- and downgoing fields as $\hat{p}^{-,+}_{sim} = \hat{p}^{-,+}_{sim}(\mathbf{x}_d, \mathbf{e}_s)$, where here $\hat{p}^{-,+}_{sim}$ are the fields that result from blending/enconding $\hat{p}^{-,+}$, with $\mathbf{e}_s$ denoting an ensemble of blended/encoded sources. All available blended-source ensembles can be combined into the wavefield matrices $\hat{\mathbf{P}}^{-,+}_{sim}$ which are related to the unblended $\hat{\mathbf{P}}^{-,+}$ using $\hat{\mathbf{P}}^{-,+}_{sim} = \hat{\mathbf{P}}^{-,+}\mathbf{B}$ where $\mathbf{B}$ is the so-called blending or encoding matrix (Wapenaar et al., 2012). For our joint wavefield approach, we first define the joint wavefield matrices for blended/encoded as, e.g.,

$$\hat{\mathbf{P}}^{-,+}_{J,sim} = \left[w_1\hat{\mathbf{P}}^-_{(1)}\mathbf{B}_{(1)} \;\; \cdots \;\; w_N\hat{\mathbf{P}}^-_{(N)}\mathbf{B}_{(N)}\right], \tag{5}$$

where $\mathbf{B}_{(1,\cdots,N)}$ are encoding matrices corresponding to experiments (1) through (N). Next, we define the joint encoding matrix to be $\mathbf{B}_J = \text{blockdiag}\left(\mathbf{B}_{(1)},\cdots,\mathbf{B}_{(N)}\right)$, i.e., a block diagonal matrix with the blending matrices of each individual experiments as its block diagonal elements. It then follows that $\hat{\mathbf{P}}^{-,+}_{J,sim} = \hat{\mathbf{P}}^{-,+}_J\mathbf{B}_J$. With these definitions, it is straightforward to verify that $\hat{\mathbf{C}}_{J,sim} = \hat{\mathbf{R}}^+_{\mathbf{0}}\hat{\Gamma}_{J,sim}$ (van der Neut et al., 2010). Thus, the inverted EIs are obtained by

$$\begin{aligned} \widehat{\mathbf{R}}^+_{\mathbf{0,LS}} &= \hat{\mathbf{C}}_{J,sim}\hat{\Gamma}^\ddagger_{J,sim} \\ &= \hat{\mathbf{P}}^-_J\mathbf{B}_J\mathbf{B}_J^\dagger\left(\hat{\mathbf{P}}^+_J\right)^\dagger\left[\hat{\mathbf{P}}^+_J\mathbf{B}_J\mathbf{B}_J^\dagger\left(\hat{\mathbf{P}}^+_J\right)^\dagger\right]^\ddagger, \end{aligned} \tag{6}$$

which is essentially the same as in the case for non-blended data (equation 4), only with appropriately modified $\mathbf{C}$ (correlation EI matrices) and Γ (the JPSF matrices). As in equation 4, $\hat{\Gamma}^\ddagger_{J,sim}$ denotes any chosen pseudoinverse of $\hat{\Gamma}_{J,sim}$. Equation 6 shows that the JPSF-based inversion fully accounts for the effects of blended/simultaneous sources in an implicit manner.

Example from dual-source vector-acoustic data

In a particular application of the JPSF system, we propose using it for inverting for broadband extended images from dual-source vector-acoustic seismic data. In that context, we have the following choices for joint wavefields:

$$\begin{aligned} \hat{\mathbf{P}}^{-,+}_{J,(s,u+g)} &= \left[\hat{\mathbf{P}}^{-,+}_{(s,u)} \quad \hat{\mathbf{P}}^{-,+}_{(s,g)}\right] \\ \hat{\mathbf{P}}^{-,+}_{J,(m+d,f)} &= \left[w_1\hat{\mathbf{P}}^{-,+}_{(m,f)} \quad w_2\hat{\mathbf{P}}^{-,+}_{(d,f)} \quad\right] \\ \hat{\mathbf{P}}^{-,+}_{J,(m+d,u+g)} &= \left[w_1\hat{\mathbf{P}}^{-,+}_{(m,u)} \quad w_1\hat{\mathbf{P}}^{-,+}_{(m,g)} \quad w_2\hat{\mathbf{P}}^{-,+}_{(d,u)} \quad w_2\hat{\mathbf{P}}^{-,+}_{(d,g)}\right], \end{aligned} \tag{7}$$

where $\hat{\mathbf{P}}^{-,+}_{J,(s,u+g)}$ indicates joint imaging using a single source type and combining ghost and upgoing fields, $\hat{\mathbf{P}}^{-,+}_{J,(m+d,f)}$ represents the combination of dual sources (monopole and dipole) for a single type of receiver data (upgoing or ghost), and finally $\hat{\mathbf{P}}^{-,+}_{J,(m+d,u+g)}$ uses joint wavefields combining both upgoing and ghost fields, from both monopole and dipole source types. Because an appropriate weighting between up- and downgoing (ghost) fields is implicitly accounted for by our receiver extrapolation scheme (see next paragraph), here the

purpose of the weights w_1 and w_2 is to account for the power balancing between the monopole and dipole source types. We thus choose the weights such that $w_2 = Kw_1$ where K is the ratio between the maximum power of the dipole and monopole source excitation functions.

We present numerical examples of broadband inversion of EIs using the proposed JPSF approach, using the layered model in Figure 1. The modeling is done using acoustic finite-difference simulations for pressure and particle velocity data. Monopole sources are modeled pressure sources with a 20Hz Ricker source pulse, dipole sources are modeled from the pressure as vertical particle-velocity point forces. Receiver wavefield extrapolation is carried out following the steps described by Vasconcelos (2013), and the receiver wavefields related to the receiver-side upgoing and ghost fields are computed in separate domains.

Figure 2 displays extended images (EIs): the top row of the figure contains correlation-based EIs (Vasconcelos et al., 2010), while in the bottom row are inverted EIs $I_e(\mathbf{x}+\delta\mathbf{x},\mathbf{x},\tau) = R_0^+(\mathbf{x}+\delta\mathbf{x},\mathbf{x},\tau)$ (Figure 1), after MDD. Figure 2 shows that the JPSF-based EIs contain fewer artifacts and are substantially more impulsive (i.e., broader bandwidth) than the one in Figure 2a. Both EIs in Figures 2b and 2c result from combining fields from dual sources, with the EI combining upgoing and ghost fields from both source types yielding the best inverted EI results. This improvement in inverted EIs results not only from using the broader-bandwidth $\hat{\mathbf{\Gamma}}_J$, but also from the increase in spatial and temporal resolution in $\hat{\mathbf{C}}_J$. When compared to the true model contrasts in Figure 1, the inverted EI in Figure 2c retrieves a reflectivity response with accurate correspondence to the model features. This includes the separation of top and bottom reflectivity signals related to a thin layer at 0.76-km depth, seen in the inverted EI gathers at approximately 0.3 s.

Finally, analogously to Figure 2, Figure 3 shows the extended images in the case of blended data. Now the 250 sources of the original experiment are blended into 50 discrete source ensembles, with time delays as indicated in the caption of Figure 3. As the top row of Figure 3 shows, the crosstalk between the simultaneous sources in the blended data introduces a strong imprint in the correlation-based EIs (compare to top row of Figure 2) that obscures the desired subsurface responses at nonzero time lags. Before deconvolution is applied, the top row of Figure 3 also shows that simply by combining multiple wavefields the simultaneous-source crosstalk is attenuated in the EIs to some extent. After MDD using the extended-image point-spread functions (middle and bottom row of Figure 3), the simultaneous-source crosstalk noise is dramatically reduced and the retrieved EIs approximate those in the case of non-blended data (Figure 2).

Conclusions

With the objective of retrieving extended images (EIs) representing reflectivity operators within the subsurface, we present a method for joint inversion of wavefields from multiple experiments for a single set of EIs. Building on the concept of wavefield PSFs used in interferometry, the inverted reflectivity-based EIs can be obtained by performing an MDD of correlation-based EIs with the appropriate joint point-spread functions (JPSF). Furthermore, we show that, by design, the JPSF formulation can fully account for blended/simultaneous-source data at the imaging condition step, with no need to separate simultaneous-source data or explicitly estimate an inverse of encoding operators prior to imaging.

When imaging dual-source vector-acoustic data, we treat source and receiver wavefields from upgoing or ghost data, from either monopole or dipole sources as four different experiments corresponding to the same subsurface. We show how these four datasets can yield different combinations of JPSF systems at depth from their corresponding extrapolated subsurface wavefields. We illustrate the broadband characteristics of the jointly inverted EIs compared to inversions using single wavefields, e.g., upgoing-only data from a single source type. The JPSF-based inversion for extended images can, in principle, handle imaging of both primaries and multiples in complex geological settings.

Acknowledgments

We thank Colin Thomson for many insights in our ongoing discussions on the properties of the reflection operator. We thank Schlumberger and WesternGeco for supporting this research. Colin Thomson, Dirk-Jan van Manen, Robin Fletcher, Amy Benedict and Kevin McGoff (all Schlumberger) were very helpful with their early reviews of this manuscript. We are thankful to Joost van der Neut (TU Delft) for discussions that have further improved this work.

References

Sava, P. and I. Vasconcelos, 2011, Extended imaging conditions for wave-equation migration: Geophysical Prospecting, **59**, 35–55.

van der Neut, J., K. Mehta, J. Thorbecke, and K. Wapenaar, 2010, Controlled-source elastic interferometric imaging by multi-dimensional deconvolution with downhole receivers below a complex overburden: SEG Technical Program Expanded Abstracts, **29**, 3979–3985.

Vasconcelos, I., 2013, Source-receiver reverse time imaging of dual source, vector-acoustic seismic data: Geophysics, in press.

Vasconcelos, I., P. Sava, and H. Douma, 2010, Nonlinear extended images via image-domain interferometry: Geophysics, **75**, SA105–SA115.

Wapenaar, K., J. van der Neut, E. Ruigrok, D. Draganov, J. Hunziker, E. Slob, J. Thorbecke, and R. Snieder, 2011, Seismic interferometry by crosscorrelation and by multidimensional deconvolution: a systematic comparison: Geophysical Journal International, **185**, 1335–1364.

Wapenaar, K., J. van der Neut, and J. Thorbecke, 2012, On the relation between seismic interferometry and the simultaneous-source method: Geophysical Prospecting, **60**, 802–823.

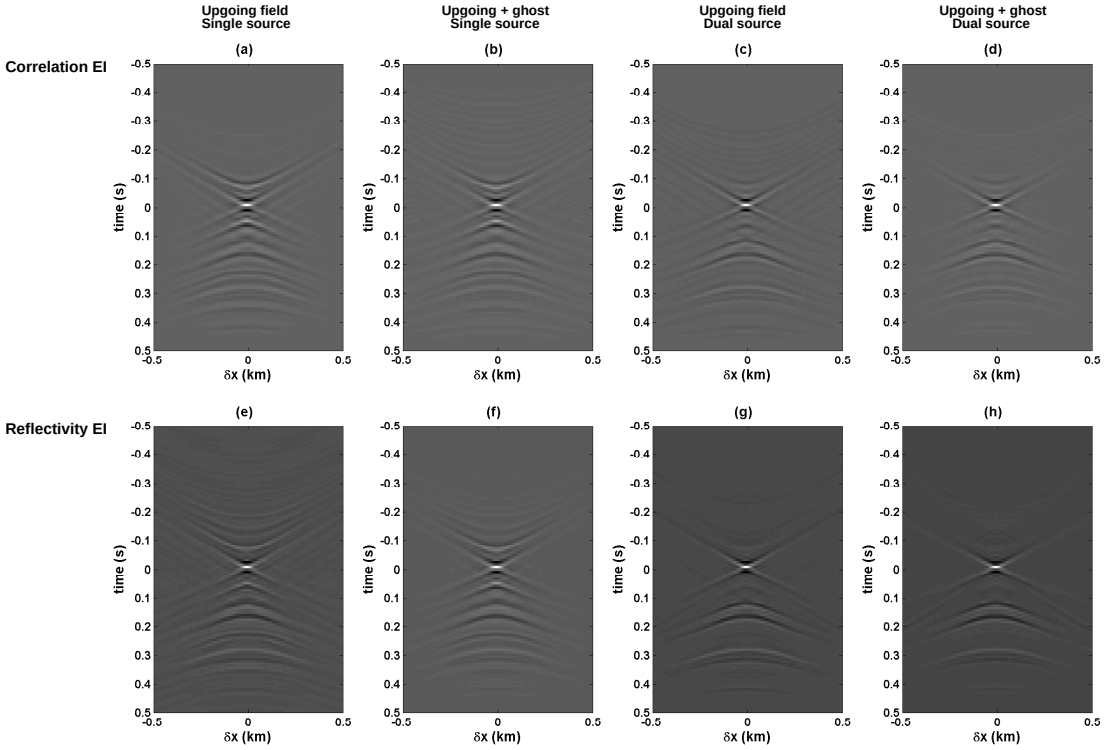

Figure 2: Comparison of correlation-based EIs (top row) with EIs after MDD (bottom row). Column-wise, the panels represent different configurations of input wavefields, as indicated above each column

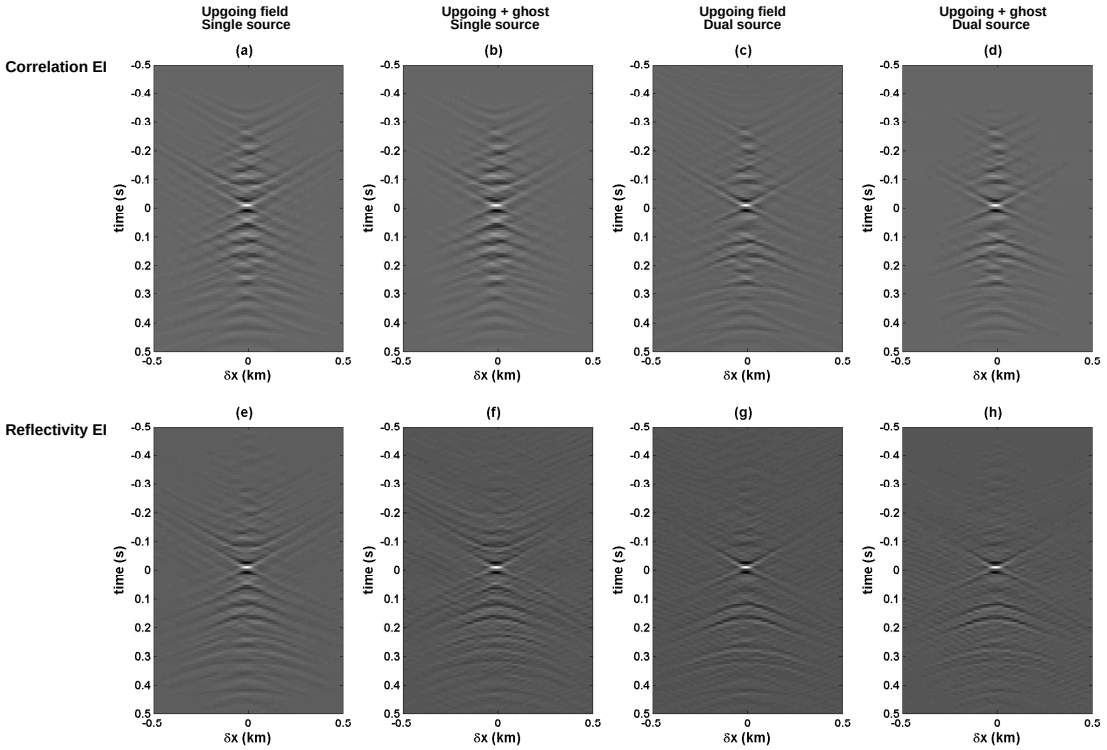

Figure 3: Same as in Figure 2, but using blended wavefields. Here, the wavefields blend every five adjacent shots from the original experiment in Figure 2 with a fixed time encoding with delays of (0.8526 s, 0.2813 s, 1.7352 s, 0.1079 s, 1.4173 s).